Improved Chemical Stability of Organometal Halide Perovskite Solar Cells Against Moisture and Heat by Ag Doping

Chaneui Park, Seok Joo Yang, Jinhyeok Choi, Sungwon Song, Wookjin Choi, and Kilwon Cho*[a]

Organometal halide perovskite (OHP) solar cells have been intensively studied because of their promising optoelectronic features, which has resulted in high power conversion efficiencies > 23%. Although OHP solar cells exhibit high power conversion efficiencies, their relatively poor stability is a significant obstacle to their practical use. We report that the chemical stability of OHP solar cells with respect to both moisture and heat can be improved by adding a small amount of Ag to the precursor. Ag doping increases the size of the OHP grains and reduces the size of the amorphous intergranular regions at the grain boundaries, and thereby hinders the infiltration of moisture into the OHP films and their thermal degradation. Quantum mechanical simulation reveals that Ag doping increases the energies of both the hydration reaction and heat-induced vacancy formation in OHP crystals. This procedure also improves the power conversion efficiencies of the resulting solar cells.

Introduction

Organometal halide perovskite (OHP) crystals are promising materials for use as active layers of next-generation solar cells. OHPs have an ABX_3 structure in which A is a monovalent organic ion such as methylammonium $CH_3NH_3^+$ (MA^+), formamidinium $(NH_2)_2CH^+$ (FA^+), or an inorganic ion such as Cs^+; B is a metal cation such as Pb^{2+} or Sn^{2+}; and X is a halogen anion such as I^-, Br^-, or Cl^-. OHPs typically have an optical band gap in the range 1.4–1.6 eV, an excellent absorption coefficient, ambipolar charge transport properties, a weak exciton binding energy, and a long charge-carrier diffusion length.[1–5] These characteristics can be tuned by varying the composition of the OHP.[6–8] The power conversion efficiencies (PCEs) of single-junction OHP solar cells have rapidly increased to > 23%,[9, 10] which is near the theoretical maximum.

However, the degradation of OHP crystals can be caused by numerous factors such as light illumination,[11–14] oxygen,[15–17] moisture,[13, 18–20] thermal energy,[21–24] and electric fields.[25, 26] The stability of OHPs has attracted relatively little attention, and the resulting lack of understanding of this instability has delayed their commercial applications. In this study, we consider the degrading effects of moisture and heat on OHPs.

The grain boundary of an OHP crystal consists of an amorphous intergranular film (IGF) that absorbs H_2O molecules much faster than the grain surface.[18] Therefore, H_2O molecules permeate the grain boundaries of OHP crystals and hydrate them to produce $MAPbI_3 \cdot H_2O$ or $(MA)_4PbI_6 \cdot H_2O$.[27, 28] This hydration is reversible, so in dry conditions the hydrates can revert to the OHP form; however, the presence of other factors such as heat or light illumination is likely to induce the irreversible degradation of OHP crystals.[29–31] Commercialization of OHP solar cells requires an ability to control the moisture-induced degradation of OHP crystals and thus improve their stability in most conditions. Recently, various methods have been tested to improve the stability of OHP crystals against moisture; examples include compositional engineering, application of a hydrophobic top interlayer, and the use of additives such as polymers, organic halide salts, inorganic acids, or ionic liquids.[32–34]

Thermal energy degrades OHP crystals to PbI_2 and other components. The operational temperature of solar cells under illumination can exceed 80°C,[35] and thermal degradation cannot be prevented by encapsulation, so the thermal stability of OHP films must be increased. At a high temperature, OHP crystals change phase from tetragonal to cubic. The length of the c-axis decreases during this transformation and induces the release of ions.[36, 37] Heat-induced ion migration in OHP crystals mainly occurs at grain boundaries, at which the chemical binding energy of atoms is approximately half that of atoms inside the crystals because these atoms are bound by only half the number of chemical bonds that bind atoms inside the crystals.[38] In particular, halogen and organic ions have a lower migration barrier than the other ions in OHPs.[39] Diffusion of iodine ions in OHPs into the hole transport layers of devices is evident at a low temperature (50°C).[22] Therefore, suppression of ion migration of OHP at its grain boundaries can be an effective way to obtain a thermally stable OHP film.[24, 40] Compositional engineering, the addition of molecular

[a] C. Park, S. J. Yang, J. Choi, S. Song, Dr. W. Choi, Prof. K. Cho
Department of Chemical Engineering
Pohang University of Science and Technology
Pohang, 37673 (Korea)
E-mail: kwcho@postech.ac.kr

Supporting Information and the ORCID identification number(s) for the author(s) of this article can be found under:
https://doi.org/10.1002/cssc.202000192.

ChemSusChem

Full Papers
doi.org/10.1002/cssc.202000192

Chemistry Europe
European Chemical
Societies Publishing

additives and ionic doping, can be used to enhance the thermal stability of OHP crystals.[24,41–45]

Doping in OHPs can tune the material properties of the crystals. Depending on the dopants' ionic radii, they become located at a substitutional or interstitial site in the OHP crystal lattice.[46] Various dopants such as K^+, Na^+, Bi^{3+}, Cu^+, and Ag^+ have been used for modifications such as adjusting the carrier concentration, tuning the position of the Fermi level, and suppressing the $J–V$ hysteresis.[47–52] However, most reports on doping have focused on the morphology, optoelectronic properties, and photovoltaic efficiencies of OHP solar cells. In this study, we exploit the fact that doping in OHPs tunes their bulk material properties, and provide a simple method to improve the chemical stability of OHP as well as the photovoltaic efficiencies of the associated solar cells.

We present Ag doping as a simple and effective way to increase the chemical stability of $(Cs_{0.05}(FA_{0.85}MA_{0.15})_{0.95})$-$Pb(I_{0.85}Br_{0.15})_3$ OHP solar cells with respect to both moisture and high temperatures. Ag was chosen as the dopant because Ag doping can also improve the photovoltaic efficiencies of OHP solar cells,[48–50] and because the ionic radius of Ag^+ (1.15 Å) is similar to that of Pb^{2+} (1.19 Å) so Ag doping should not severely distort the OHP crystal structure. The Ag doping concentration was optimized to increase the moisture and thermal stability as well as the PCE of OHP solar cells. To understand the stabilizing effects of Ag, we examined the OHP film morphology and performed density functional theory (DFT) calculations to quantify the energy of vacancy formation by ion migration and the energy of the hydration reaction. The mechanism by which Ag doping improved moisture and thermal stability of OHP solar cells was systematically investigated.

Results and Discussion

We fabricated OHP solar cells with the cell structure fluorine-doped tin oxide (FTO)/SnO$_2$/(Cs$_{0.05}$(FA$_{0.85}$MA$_{0.15}$)$_{0.95}$)Pb(I$_{0.85}$Br$_{0.15}$)$_3$/2,2′,7,7′-tetrakis[N,N-di(4-methoxyphenyl)amino]-9,9′-spirobi-fluorene (spiro-MeOTAD)/Au. Perovskite films were fabricated using a method that was modified from a previous study.[42] Mixing appropriate amounts of a pristine OHP precursor and an OHP precursor containing 1 mol% AgI yielded Ag-doped OHP solar cells that had the same structure as the undoped cells.

We fabricated and optimized perovskite solar cells by varying the Ag content ([Ag], in mol%). The $J–V$ curves of the champion solar cells with [Ag] = 0, 0.1, or 0.3 are shown in Figure 1a. The PCEs were distributed approximately normally; the average PCE was the highest for the cell with [Ag] = 0.1 (Figure 1b, Figure S1). The most efficient pristine cells had a PCE = 19.0%, and [Ag] = 0.1 achieved the highest PCE = 19.7% (Table 1). These results indicated that Ag doping increases the PCE of the associated solar cells. This increase in the PCE of
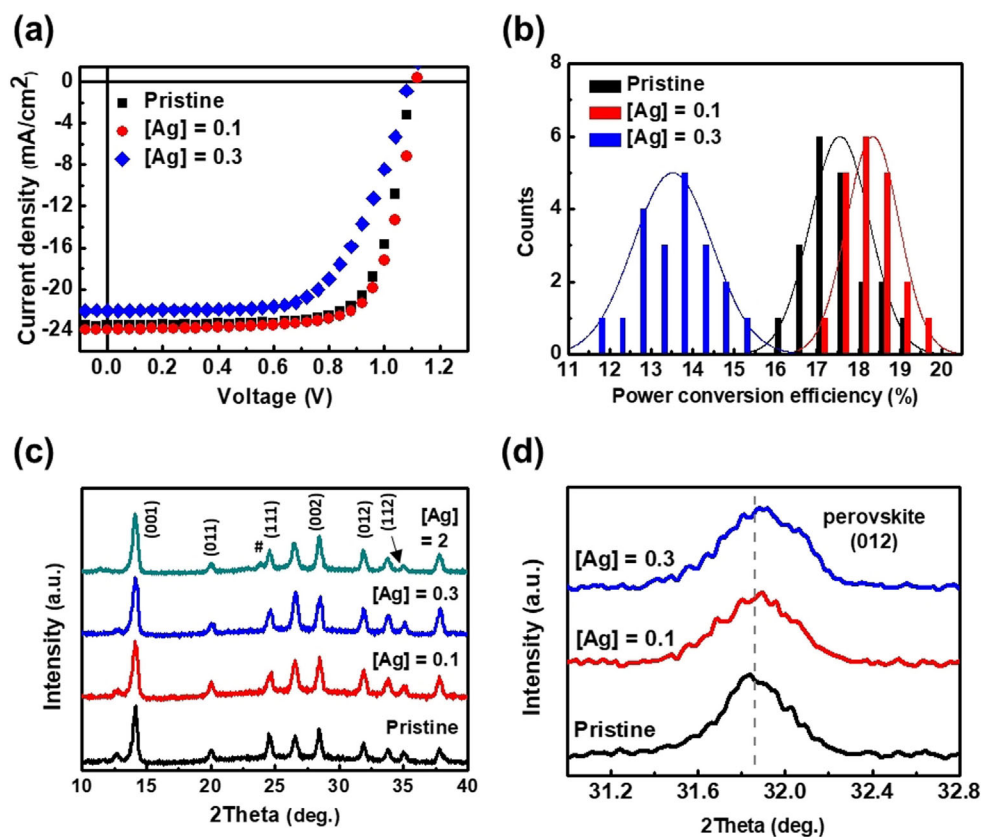

Figure 1. (a) $J–V$ curves of champion solar cells using OHP doped with Ag concentrations ([Ag], mol%) = 0, 0.1, or 0.3. (b) PCE distributions of optimized solar cells with [Ag] = 0, 0.1 or 0.3. (c) XRD patterns of OHP films with various [Ag]. #: new crystalline phase caused by high [Ag]. The intensities of the XRD patterns were normalized by the intensities of the OHP (100) peak of each pattern. (d) OHP (012) XRD peak for OHP films with [Ag] = 0, 0.1 or 0.3.

⭦⭦ These are not the final page numbers!

Table 1. Electrical data of the champion OHP solar cells with and without Ag doping.

Ag content [mol%]	PCE [%]	J_{SC} [mA cm^{-2}]	V_{OC} [V]	FF
0	19.0	23.4	1.10	0.74
0.1	19.7	23.8	1.12	0.74
0.3	15.3	22.1	1.10	0.63

the OHP solar cell upon addition of the optimized [Ag] was attributed to the improved film morphology, as discussed below, to improved carrier dynamics, and to reduced excessive electron concentrations for balanced charge transport.[48,49] However, further increases in [Ag] decreased the PCEs of the associated solar cells (Figure 1b, Figure S1). The decrease in the PCE upon excessive [Ag] resulted from a downward shift of the HOMO and LUMO levels and an increase in nonradiative recombination in the OHP films.[48]

The XRD patterns of the OHP films with [Ag] = 0, 0.1, or 0.3 were very similar; this result indicated that the use of [Ag] = 0.1 and 0.3 did not affect the OHP crystalline structure or produce other crystalline phases (Figure 1c). However, the use of [Ag] = 2.0 did produce a new crystalline phase at $2\theta = 23.9°$ in the XRD pattern; this result indicated that the addition of excess [Ag] induced segregation of the crystal phases.

Cross-sectional TEM and electron energy loss spectroscopy (EELS) (Figure S2, Supporting Information) revealed that Ag was homogeneously distributed in the OHP films and that it does not accumulate in regions such as the grain boundaries. At the molecular level, Ag dopant could be present in the OHP crystal lattice by substituting at A or B sites, or by settling onto interstitial positions. To investigate the chemical states of the constituting elements in OHP films, X-ray photoelectron spectroscopy (XPS) spectra of OHP films with [Ag] = 0, 0.1, or 1 were obtained (Figure S3). Ag doping induced the shifts of both Pb 4f and I 3d XPS peaks. Because simple physical mixing could not cause any remarkable chemical state change,[53]

these shifts were evidence of the changes in the chemical bonding of the lead cations and iodide anions in the perovskite. Furthermore, the shift of the OHP XRD (012) peak can be used as an indicator of lattice contraction or expansion in small scale,[46] because it reflects a smaller *d*-spacing than the peaks that appear at lower angles. The addition of Ag increased the angle of the XRD (012) peak of OHP (Figure 1d). The centers of the (012) peak for OHP films were 31.86° at [Ag] = 0, 31.87° at [Ag] = 0.1, and 31.89° at [Ag] = 0.3. This increase in peak angle was consistent with a contraction of the crystal lattice. This result ruled out interstitial Ag doping because the presence of interstitial dopants would induce repulsion of adjacent atoms and thereby expand the crystal lattice. The ionic radius of Ag$^+$ is 1.15 Å; therefore, Ag$^+$ was more likely to replace Pb^{2+} (radius = 1.19 Å) than FA$^+$ (2.79 Å) because of the similar size, which is consistent with previous reports.[48]

We measured the effects of Ag doping on the resistance to moisture and heat of the associated OHP solar cells. In general, the water contact angle (θ_C) of the OHP film decreases as H_2O-induced degradation of OHP films proceeds.[54] We fabricated OHP films with [Ag] = 0, 0.1, or 0.3 and measured their θ_C (Figure 2a). The measurements were completed in 1 s after applying the drop of water. The measured θ_C were 53.5° at [Ag] = 0, 60.3° at [Ag] = 0.1, and 63.6° at [Ag] = 0.3. The increase in θ_C of the OHP films was contributed by retarded hydration, which indicated that Ag doping improved the resistance of the OHP films to H_2O-induced decomposition. Therefore, Ag doping was also expected to slow the moisture-induced degradation of the PCEs of the associated OHP solar cells (Figure 2b).

We confirmed that Ag doping does indeed improve the moisture stability of OHP solar cells. We stored OHP solar cells with [Ag] = 0, 0.1, or 0.3 in ambient air with 65% relative humidity at room temperature and measured the PCEs of the cells as a function of the storage time. After storage for 1000 h, the retained percentage of initial PCE was 29% for pristine solar cells with [Ag] = 0, 58% for cells with [Ag] = 0.1, and
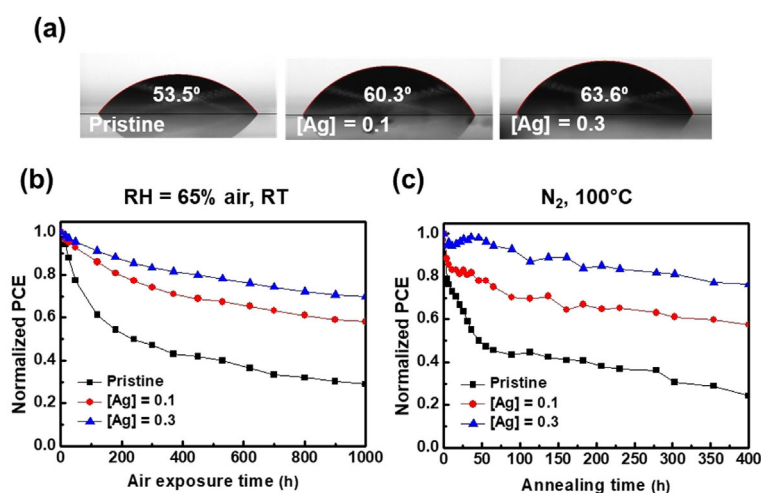

Figure 2. (a) Contact angles (θ_C) of a water drop on OHP films containing Ag concentrations ([Ag], mol%) 0, 0.1 or 0.3. θ_C was measured within 1 s after water was dropped on the OHP films. Normalized power-conversion efficiencies of OHP solar cells containing [Ag] = 0, 0.1 or 0.3 as a function of (b) storing time at room temperature in ambient air with RH = 65%, and (c) thermal annealing time at 100 °C in a N_2-filled glove box.

These are not the final page numbers! ↗↗

ChemSusChem

Full Papers
doi.org/10.1002/cssc.202000192

Chemistry Europe
European Chemical
Societies Publishing

70% for cells with [Ag]=0.3. Note that the stabilization increased as the dopant concentration increased.

Ag doping also improved the thermal stability of OHP solar cells (Figure 2c). We measured the PCEs of OHP solar cells containing [Ag]=0, 0.1, or 0.3 as a function of time during thermal annealing at 100°C in a N_2-filled glove box. The overall trend pf the PCEs was analogous to that found for moisture-induced degradation. Interestingly, the cells with [Ag]=0.3 showed increases in PCE during the early stage of thermal annealing (≈50 h). This result can be caused by diffusion of spiro-MeOTAD into the perovskite layer. The diffusion of spiro-MeOTAD passivates trap states at perovskite grain boundaries and increases carrier-extraction efficiency, and this change leads to an increase in PCE of the associated solar cell.[55] For the cells with [Ag]=0.1, the PCE decay showed a small plateau at the early stage of thermal annealing (≈25 h); which could be owing to the same cause. OHP solar cells were subjected to thermal annealing at 100°C for 400 h; the resulting PCEs (compared with the initial) were 24%, 58%, and 76% in cells containing [Ag]=0, [Ag]=0.1, and [Ag]=0.3, respectively. This result indicated that the addition of Ag improved both the thermal stability and the moisture stability of the associated OHP solar cells.

We demonstrated that the increase in the concentration of Ag dopant improves the stability of OHP solar cells against moisture and heat. However, excessive Ag doping decreases the PCE of the resulting solar cells. These results imply that the dopant concentration should be optimized to obtain OHP solar cells that are both highly stable and efficient. In this study, we claim that [Ag]=0.1 is the optimal concentration to improve the stability of OHP solar cells without the loss of PCE.

We studied the effects of Ag doping on the crystal morphologies of the OHP films to determine the origin of these improvements. We fabricated OHP films containing [Ag]=0, 0.1, 0.2, 0.3, 0.5, 1, or 2; their SEM images are shown in Figure S4. The average grain sizes $\bar{G}$ of the OHP films were determined from the SEM images by using the ASTM E112 intercept procedure (Table S1 and Supplementary Note 1). As [Ag] increased, $\bar{G}$ of the OHP films gradually increased (Figure 3a) from 156 nm in the OHP film with [Ag]=0 to 398 nm in film with [Ag]=2. Ag doping slows the dark-phase formation of the perovskite; the slowing reduces the number of nuclei during the perovskite crystallization and thereby increases the size of crystal grains.[49] In general, the grain boundary in an OHP is the main pathway of H_2O infiltration and is also vulnerable to heat-induced ion migration. An increase in $\bar{G}$ results in a decrease in the surface area of the grain boundary, and thereby reduces the area through which H_2O molecules can infiltrate. Therefore, the increase in $\bar{G}$ owing to Ag doping improves the moisture stability of the OHP films by reducing the H_2O infiltration area.

The increase in $\bar{G}$ was also correlated with the improved thermal stability of the OHP solar cells. Compared with atoms inside grains, atoms located at grain boundaries are involved in fewer chemical bonds and are more likely to migrate in response to thermal energy. The increase in $\bar{G}$ owing to Ag doping reduces the overall interfacial area of the grain boun-
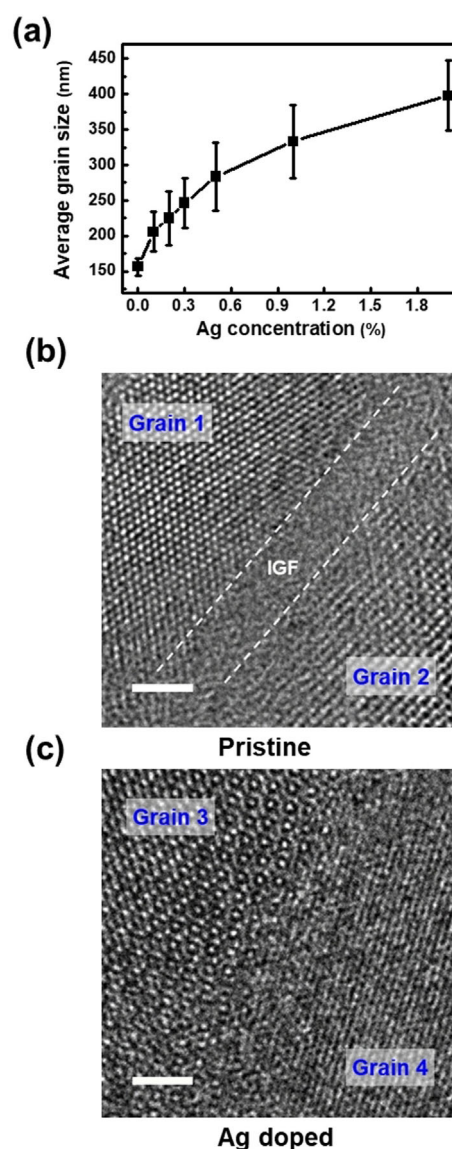

Figure 3. (a) Average grain size of OHP films as a function of Ag concentration. TEM images of OHP films (b) without Ag, and (c) with [Ag]=0.3. Scale bar: 2 nm.

dary and, as a result, improves the thermal stability of the associated OHP solar cells.

The crystal morphology near the OHP grain boundaries was investigated by using TEM. OHP films have an approximately 5-nm-thick amorphous IGF composed of unreacted OHP precursors, impurities, and other components.[18] The IGF allows quick infiltration of H_2O into the OHP films. TEM images were obtained of regions near the grain boundaries of OHP films without Ag and with Ag doping (Figures 3b,c; fast Fourier transformation patterns Figure S5). The pristine OHP film had a 2- to 3-nm-thick IGF between grains (Figure 3b), whereas the OHP film with Ag had almost no IGF (Figure 3c and Figure S6). Ag doping was presumed to tune the composition of the perovskite films (not the composition of the OHP precursor) so that it was more stoichiometric, which means that unreacted OHP precursor was removed. This result was consistent with

↖↖ **These are not the final page numbers!**

ChemSusChem

Full Papers
doi.org/10.1002/cssc.202000192

Chemistry Europe
European Chemical
Societies Publishing

the decrease in the XRD peak intensities of PbI_2 as the Ag concentration increased (Figure S7). Therefore, Ag doping of OHP films prevents the formation of the IGF and thus suppresses H_2O infiltration into the films. This effect hinders moisture-induced degradation of OHP films.

We conducted a quantum mechanical simulation with DFT to calculate the energies of the hydration reaction at the OHP surface and of the vacancy formation caused by temperature-induced ion migration. A 2×1 OHP slab with three (001)-plane layers was used to calculate the surface hydration reaction energy, and a $2\times2\times2$ cubic OHP supercell was built to calculate the vacancy formation energy E_{VF} (Figure S8).

The simulations were used to calculate the hydration reaction energies, the distance from O atoms to Pb atoms, and the net charge of H_2O on the hydrated pristine and Ag-doped OHP structures; the intent was to investigate the moisture stabilization effects of Ag doping. A Pb–I-terminated OHP slab, which is dominant in PbI_2-excessive systems,[56,57] was constructed. H_2O forms a chemical bond with Pb at the crystal surface to produce the OHP hydrate.[58] The hydration reaction energy was −0.32 eV for pristine OHP, and −0.2 eV for Ag-doped OHP (Figure 4a). For the pristine structure, the calculated O−Pb distance was 2.720 Å and the net charge of H_2O was $0.4e$, whereas for the Ag-doped structure the calculated O−Pb distance was 2.765 Å and the net charge was $0.1e$ (Table 2). The increased O−Pb distance and the reduced net charge of H_2O

molecules of the Ag-doped perovskite indicate that the interaction between H_2O and the perovskite surface was weakened, so the energy barrier to hydration increased. These results indicated that the hydration reaction was less favorable in Ag-doped OHP than in pristine OHP; this difference explains the improved moisture stability of the associated OHP solar cells.

Activation energies for ion migration in OHP are lower for organic ions and halogen ions than for Pb^{2+}; therefore, organic ions and halogen ions are more likely to migrate than Pb^{2+}.[39] To obtain the E_{VF} of temperature-induced ion migration, a FA^+ and I^- were removed from the supercell to satisfy the ionic compensation of the charged point defects (Figure 4b).[59,60] E_{VF} were calculated for several possible FA^+ and I^- vacancy sites in the supercell structure and the one with the lowest energy was chosen. The obtained E_{VF} for FA^+ and I^- vacancies in pristine OHP was 2.17 eV. To investigate the E_{VF} of Ag-doped OHP, one Pb^{2+} ion was replaced with a Ag^+ ion, and one I^- ion was removed to ensure charge neutrality. For Ag-doped OHP, the calculated E_{VF} for FA^+ and I^- vacancies was 2.68 eV. This increase in E_{VF} for the Ag-doped OHP over that of the pristine OHP indicated that vacancy formation was suppressed in Ag-doped OHP, and suggested that Ag doping hindered temperature-induced ion migration by increasing the E_{VF}, and this increase improved the thermal stability of the associated OHP films. The increased barrier for ion vacancy formation was attributed to the relaxation of lattice stress in the crystal by the incorporation of the small Ag ion in the OHP.[61–65]

Decomposition enthalpy can be used to explain the improved stability of the Ag-doped perovskite.[66] The calculated decomposition enthalpy was higher in the doped perovskite (1.38 eV/atom) than in the pristine perovskite (1.31 eV/atom) (Table 2); this difference indicated that the Ag doping increases the thermal stability of the perovskite.

The addition of Ag to an OHP is heterovalent doping; the presence of the Ag dopant in the OHP crystal might induce the formation of vacancies that result in trap states, or might reduce ion migration barriers. In fact, in OHPs, Ag has a lower coordination number than Pb.[48] To investigate the influences of Ag doping on the trap density and ion migration in the OHP films, the trap-filled-limit voltages V_{TFL} and capacitance–frequency (C--f) plots were obtained for OHP solar cells with [Ag]=0, 0.1, or 0.3 (Figures 5a,b and Figure S10).

The V_{TFL} values of electron-only and hole-only devices with the various Ag concentrations were determined in each case at the kink point, at which the increase in the dark current as a function of voltage in a log–log scale changes from a slope of 1 to a slope >3. Electron-only devices had $V_{TFL}=0.45$ V at [Ag]=0, and 0.27 V at both [Ag]=0.1 and [Ag]=0.3 (Figure 5a); hole-only devices had $V_{TFL}=0.27$ V at [Ag]=0, 0.23 V at [Ag]=0.1, and 0.22 V at [Ag]=0.3 (Figure 5b). The trap density is proportional to V_{TFL}, so these decreases in V_{TFL} with increase in [Ag] revealed that Ag doping of the OHP films reduced their trap densities; this result was consistent with the increase in V_{OC} of a device with [Ag]=0.1.[67] We conclude that the reduction in the total area of the OHP grain boundaries owing to Ag doping yielded a reduction in the trap density, and we presume that this phenomenon overwhelms the ef-
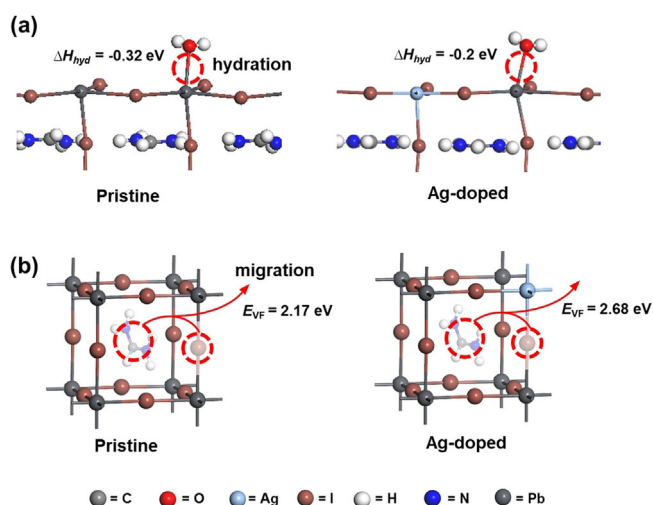

Figure 4. Diagram of (a) hydration and (b) the FA^+ and I^- vacancy formation of pristine and Ag-doped OHP. The heat of formations was obtained by DFT calculations.

Table 2. Calculated hydration energy (E_{hyd}), distance between the O and Pb atoms, net charges of H_2O, and decomposition enthalpy of pristine and Ag-doped perovskites.

Perovskite	E_{hyd} [eV]	Distance [Å] O–Pb	Net charges H_2O [e]	Decomposition enthalpy [eV]
pristine	−0.32	2.720	0.40	1.31
Ag-doped	−0.20	2.765	0.10	1.38

ChemSusChem

Full Papers
doi.org/10.1002/cssc.202000192

Chemistry Europe
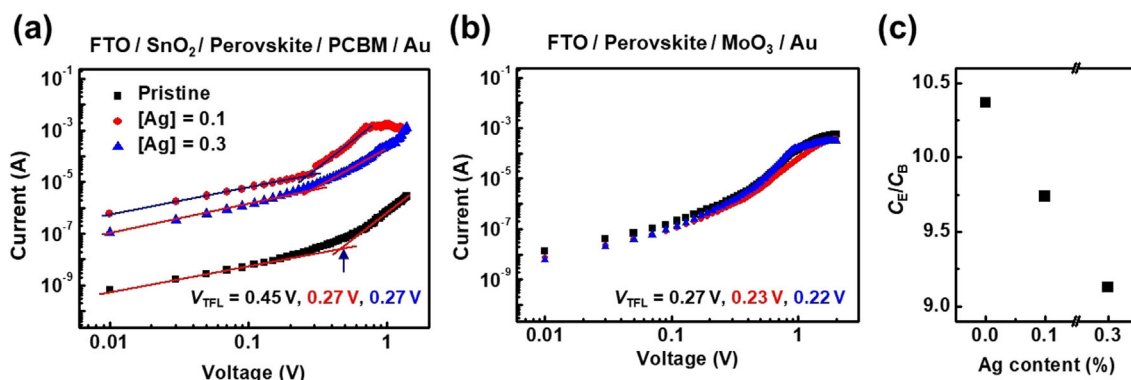European Chemical
Societies Publishing

Figure 5. Current–voltage curves of (a) electron-only and (b) hole-only devices containing Ag concentrations ([Ag], mol%) = 0, 0.1 or 0.3 in darkness (fitting lines of (b) in Figure S9). (c) C_E/C_B values of OHP solar cells containing [Ag] = 0, 0.1 or 0.3. C_E: capacitance at 10^0; C_B: capacitance at 10^4 Hz.

fects of the traps that form as a result of the heterovalent Ag doping.

C–f plots were obtained for the OHP devices with [Ag] = 0, 0.1 or 0.3 to determine whether disruption of the coordination by heterovalent Ag doping stimulated ion migration in the OHP crystal (Figure S10). Capacitances in the low-frequency region ($<10^3$ Hz) were attributed to electrode polarization caused by ion migration, whereas capacitances in the high-frequency region (10^4–10^5 Hz) were attributed to bulk properties including organic cation and PbI_6 octahedral reorientation in the OHP.[68,69] The ion migration discussed here was not identical to that discussed above in the context of our DFT calculations: the degree of ion migration obtained from C–f plots was caused by more phenomena than that discussed in the DFT simulations, which considered only the vacancy formation caused by FA^+ and I^- migration.

To quantify the degree of ion migration in the OHP films, the capacitance C_E owing to the electron polarization at 10^0 Hz C_E was divided by the capacitance C_B that is a result of the bulk properties at 10^4 Hz (Figure 5c). An increase in [Ag] reduced the C_E/C_B ratio; this change indicated that ion migration was reduced by the addition of Ag. We presume that the reduced ion migration resulted from the increased grain size of the Ag-doped OHP films. Results for both V_{TFL} and C–f confirmed that Ag doping reduced both the trap density and ion migration in the OHP films.

Conclusions

A simple and effective method was developed to suppress the degradation of OHP films by moisture and heat. By investigating the morphological and thermodynamic mechanisms, we systematically studied the stabilization of OHP by Ag doping. Ag in the OHP precursor dopes the B sites in the OHP crystals. Ag doping also increases the grain sizes of OHP films, and reduces the size of the amorphous IGF at OHP grain boundaries. The increased grain size reduces the level of heat-induced ion migration and the size of the grain interface through which H_2O molecules infiltrate; the elimination of the IGF suppresses the hydration of the OHP crystal. Ag doping also increases the barriers to hydration and heat-induced ion migration. These ef-

fects of Ag doping improve the moisture and thermal stability of OHP films in the associated solar cells. Doping of OHP films with an optimized amount of Ag can be used to obtain both highly stable and efficient OHP solar cells.

Experimental Section

Materials

PbI_2, $PbBr_2$, CsI, tin(II) chloride dihydrate, bis(trifluoromethylsulfonyl)imide lithium salt, 4-tert-butylpyridine (TBP), and all solvents used in this study were purchased from Sigma–Aldrich. Formadinium iodide (FAI) and methylammonium bromide (MABr) were purchased from GreatCell Solar. Spiro-MeOTAD was purchased from MS Solution.

OHP solar cell fabrication

0.07 M of tin chloride dihydrate in ethanol was spin-coated onto FTO glass at 3000 rpm for 30 s, followed by thermal annealing at 200 °C for 1 h to prepare FTO/SnO_2 substrates. Pristine OHP precursor solutions containing 1.1 M PbI_2, 1 M FAI, 0.15 M $PbBr_2$, and 0.15 M MABr in 4:1 (v/v) dimethylformamide/dimethyl sulfoxide (DMF/DMSO). MABr were kept on a hot plate at 60 °C. An AgI-concentrated precursor solution was prepared (1.1 M PbI_2, 1 M FAI, 0.15 M MABr, 0.15 M $PbBr_2$, and 0.1 M AgI in 4:1 (v/v) DMF/DMSO). Then 5 vol.% of 1.5 M CsI solution in DMSO was added to the precursors 1 h prior to the spin coating process. The pristine solution and the concentrated solution were mixed together to prepare diluted Ag-doped precursor solutions before spin coating. The precursor solutions on the substrate were spin-coated at 1000 rpm for 5 s, then at 6000 rpm for 20 s. Then, 150 μL chlorobenzene was poured on the spinning substrate 12 s before the end of the spinning. The OHP films were annealed at 100 °C for 1 h. A solution of 43.5 mg of spiro-MeOTAD in 0.6 mL chlorobenzene was prepared and doped with Li-TFSI and TBP. The molar ratio of the dopants for spiro-MeOTAD was 0.5 for Li-TFSI and 3.3 for TBP. After the OHP annealing, the spiro-MeOTAD solution was dropped on the substrates and spin-coated at 4000 rpm for 30 s. The films were stored in dried air overnight before electrode deposition. A 60-nm-thick Au layer for electrodes was thermally deposited under vacuum $<10^{-6}$ Torr.

⭲⭲ These are not the final page numbers!

Solar cell measurements

J–V measurements were conducted in a N_2-filled glove box under AM 1.5G illumination with an intensity of 100 mW cm^{-2} by using a Keithley 2400 and an Oriel 1 kW solar simulator referenced to a Reference Cell PVM 132 calibrated at the US National Renewable Energy Laboratory. A mask (area = 0.0555 cm^{-2}) was used for the electrode deposition. *J–V* plots were measured in the backward direction. *C–f* measurements were conducted in darkness by using a MFIA Impedance Analyzer. Over 20 cells were tested at each experimental condition.

Thin film characterization

The XRD patterns were obtained using a Rigaku D/Max-2500 diffractometer. Contact angles were measured using a Femtofab SmartDrop analyzer. SEM were obtained using a Hitachi S-4800; TEM images were obtained using a JOEL JEM-2200FS. To prepare the TEM specimens, each sample was processed using a dual beam FIB (FEI Helios).

Computational methods

DFT calculations were performed at the level of GGA in the Perdew–Burke–Ernzerhof parameterization as implemented in CASTEP from Materials Studio 2018.[70] For all calculations, electron-ion interactions were described by the on-the-fly generated ultrasoft pseudopotentials with electrons from H 1s; C and N 2s, 2p; Ag 4s, 4p, 4d, 5s; I 5s, 5p; and Pb 5s, 5p, 5d, 6s, 6p shells included in the calculations. Unless specified otherwise, 2×1 slabs with vacuum thickness of 18 Å and three OHP (001) layers, or 2×2×2 supercells of cubic structures were built and allowed to fully relax (cell shape, volume, and ion positions) by geometric optimization. An energy cutoff of 570 eV and 2×1×1 k-point meshes for the 2×1 slabs and 2×2×2 k-point meshes for the 2×2×2 supercells, were used to achieve n energy of 1×10^{-5} eV/atom, force of 0.03 eV Å^{-1}, and displacement convergence of 0.001 Å. The decomposition enthalpy was calculated by subtracting the energies of the decomposed products PbI_2, FAI, and AgI (only for the Ag-doped perovskite) from the energy of the perovskite.

Acknowledgements

Conflict of interest

The authors declare no conflict of interest.

Keywords: crystal engineering · doping · moisture stability · perovskite solar cells · thermal stability

[1] N. G. Park, *Mater. Today* **2015**, *18*, 65.
[2] H. J. Snaith, *J. Phys. Chem. Lett.* **2013**, *4*, 3623.
[3] H. Z. Lu, H. T. Zhang, S. J. Yuan, J. Wang, Y. Q. Zhan, L. R. Zheng, *Phys. Chem. Chem. Phys.* **2017**, *19*, 4516.
[4] S. D. Yang, W. F. Fu, Z. Q. Zhang, H. Z. Chen, C. Z. Li, *J. Mater. Chem. A* **2017**, *5*, 11462.
[5] S. S. Li, Y. C. Wang, C. M. Tsai, C. Y. Wen, C. H. Yu, Y. P. Yang, J. C. Lin, D. Y. Wang, C. C. Chen, Y. C. Yeh, C. W. Chen, *Nanoscale* **2015**, *7*, 14532.
[6] D. P. McMeekin, G. Sadoughi, W. Rehman, G. E. Eperon, M. Saliba, M. T. Horantner, A. Haghighirad, N. Sakai, L. Korte, B. Rech, M. B. Johnston, L. M. Herz, H. J. Snaith, *Science* **2016**, *351*, 151.
[7] N. J. Jeon, J. H. Noh, W. S. Yang, Y. C. Kim, S. Ryu, J. Seo, S. I. Seok, *Nature* **2015**, *517*, 476.
[8] S. J. Yang, M. Kim, H. Ko, D. H. Sin, J. H. Sung, J. Mun, J. Rho, M. H. Jo, K. Cho, *Adv. Funct. Mater.* **2018**, *28*, 1804067.
[9] NREL, Efficiency chart, https://www.nrel.gov/pv/ (accessed: Mar 2019).
[10] W. S. Yang, B. W. Park, E. H. Jung, N. J. Jeon, Y. C. Kim, D. U. Lee, S. S. Shin, J. Seo, E. K. Kim, J. H. Noh, S. I. Seok, *Science* **2017**, *356*, 1376.
[11] H. Tsai, R. Asadpour, J. C. Blancon, C. C. Stoumpos, O. Durand, J. W. Strzalka, B. Chen, R. Verduzco, P. M. Ajayan, S. Tretiak, J. Even, M. A. Alam, M. G. Kanatzidis, W. Nie, A. D. Mohite, *Science* **2018**, *360*, 67.
[12] E. T. Hoke, D. J. Slotcavage, E. R. Dohner, A. R. Bowring, H. I. Karunadasa, M. D. McGehee, *Chem. Sci.* **2015**, *6*, 613.
[13] D. Bryant, N. Aristidou, S. Pont, I. Sanchez-Molina, T. Chotchuangchutchaval, S. Wheeler, J. R. Durrant, S. A. Haque, *Energy Environ. Sci.* **2016**, *9*, 1850.
[14] D. W. Dequilettes, W. Zhang, V. M. Burlakov, D. J. Graham, T. Leijtens, A. Osherov, V. Bulovic, H. J. Snaith, D. S. Ginger, S. D. Stranks, *Nat. Commun.* **2016**, *7*, 11683.
[15] T. Leijtens, R. Prasanna, A. Gold-Parker, M. F. Toney, M. D. McGehee, *Acs Energy Lett.* **2017**, *2*, 2159.
[16] N. Aristidou, I. Sanchez-Molina, T. Chotchuangchutchaval, M. Brown, L. Martinez, T. Rath, S. A. Haque, *Angew. Chem. Int. Ed.* **2015**, *54*, 8208; *Angew. Chem.* **2015**, *127*, 8326.
[17] N. Aristidou, C. Eames, I. Sanchez-Molina, X. N. Bu, J. Kosco, M. S. Islam, S. A. Haque, *Nat. Commun.* **2017**, *8*, 15218.
[18] Q. Wang, B. Chen, Y. Liu, Y. H. Deng, Y. Bai, Q. F. Dong, J. S. Huang, *Energy Environ. Sci.* **2017**, *10*, 516.
[19] J. A. Christians, P. A. M. Herrera, P. V. Kamat, *J. Am. Chem. Soc.* **2015**, *137*, 1530.
[20] J. M. Frost, K. T. Butler, F. Brivio, C. H. Hendon, M. van Schilfgaarde, A. Walsh, *Nano Lett.* **2014**, *14*, 2584.
[21] A. Dualeh, P. Gao, S. I. Seok, M. K. Nazeeruddin, M. Grätzel, *Chem. Mater.* **2014**, *26*, 6160.
[22] G. Divitini, S. Cacovich, F. Matteocci, L. Cina, A. Di Carlo, C. Ducati, *Nat. Energy* **2016**, *1*, 15012.
[23] B. Conings, J. Drijkoningen, N. Gauquelin, A. Babayigit, J. D'Haen, L. D'Olieslaeger, A. Ethirajan, J. Verbeeck, J. Manca, E. Mosconi, F. De Angelis, H. G. Boyen, *Adv. Energy Mater.* **2015**, *5*, 1500477.
[24] C. Park, H. Ko, D. H. Sin, K. C. Song, K. Cho, *Adv. Funct. Mater.* **2017**, *27*, 1703546.
[25] S. Bae, S. Kim, S. W. Lee, K. J. Cho, S. Park, S. Lee, Y. Kang, H. S. Lee, D. Kim, *J. Phys. Chem. Lett.* **2016**, *7*, 3091.
[26] Y. B. Yuan, Q. Wang, Y. C. Shao, H. D. Lu, T. Li, A. Gruverman, J. S. Huang, *Adv. Energy Mater.* **2016**, *6*, 1501803.
[27] J. B. Huang, S. Q. Tan, P. D. Lund, H. P. Zhou, *Energy Environ. Sci.* **2017**, *10*, 2284.
[28] A. M. A. Leguy, Y. Hu, M. Campoy-Quiles, M. I. Alonso, O. J. Weber, P. Azarhoosh, M. van Schilfgaarde, M. T. Weller, T. Bein, J. Nelson, P. Docampo, P. R. F. Barnes, *Chem. Mater.* **2015**, *27*, 3397.
[29] W. X. Huang, J. S. Manser, P. V. Kamat, S. Ptasinska, *Chem. Mater.* **2016**, *28*, 303.
[30] B. A. Chen, J. T. Lin, N. T. Suen, C. W. Tsao, T. C. Chu, Y. Y. Hsu, T. S. Chan, Y. T. Chan, J. S. Yang, C. W. Chiu, H. M. Chen, *ACS Energy Lett.* **2017**, *2*, 342.
[31] N. Ahn, K. Kwak, M. S. Jang, H. Yoon, B. Y. Lee, J. K. Lee, P. V. Pikhitsa, J. Byun, M. Choi, *Nat. Commun.* **2016**, *7*, 13422.
[32] M. Kim, S. G. Motti, R. Sorrentino, A. Petrozza, *Energy Environ. Sci.* **2018**, *11*, 2609.
[33] W. J. Yin, Y. F. Yan, S. H. Wei, *J. Phys. Chem. Lett.* **2014**, *5*, 3625.

These are not the final page numbers! ↗↗

[34] Y. C. Zhao, J. Wei, H. Li, Y. Yan, W. K. Zhou, D. P. Yu, Q. Zhao, *Nat. Commun.* **2016**, *7*, 10228.

[35] T. A. Berhe, W. N. Su, C. H. Chen, C. J. Pan, J. H. Cheng, H. M. Chen, M. C. Tsai, L. Y. Chen, A. A. Dubale, B. J. Hwang, *Energy Environ. Sci.* **2016**, *9*, 323.

[36] G. E. Eperon, S. D. Stranks, C. Menelaou, M. B. Johnston, L. M. Herz, H. J. Snaith, *Energy Environ. Sci.* **2014**, *7*, 982.

[37] J. W. Lee, D. J. Seol, A. N. Cho, N. G. Park, *Adv. Mater.* **2014**, *26*, 4991.

[38] Y. B. Yuan, J. S. Huang, *Acc. Chem. Res.* **2016**, *49*, 286.

[39] C. Eames, J. M. Frost, P. R. F. Barnes, B. C. O'Regan, A. Walsh, M. S. Islam, *Nat. Commun.* **2015**, *6*, 7497.

[40] C. H. Chiang, C. G. Wu, *ChemSusChem* **2016**, *9*, 2666.

[41] Y. Lin, Y. Bai, Y. J. Fang, Z. L. Chen, S. Yang, X. P. Zheng, S. Tang, Y. Liu, J. J. Zhao, J. S. Huang, *J. Phys. Chem. Lett.* **2018**, *9*, 654.

[42] M. Saliba, T. Matsui, J. Y. Seo, K. Domanski, J. P. Correa-Baena, M. K. Nazeeruddin, S. M. Zakeeruddin, W. Tress, A. Abate, A. Hagfeldt, M. Grätzel, *Energy Environ. Sci.* **2016**, *9*, 1989.

[43] T. Matsui, T. Yamamoto, T. Nishihara, R. Morisawa, T. Yokoyama, T. Sekiguchi, T. Negami, *Adv. Mater.* **2019**, *31*, 1806823.

[44] S. Li, Z. F. Shi, F. Zhang, L. T. Wang, Z. Z. Ma, D. W. Yang, Z. Q. Yao, D. Wu, T. T. Xu, Y. T. Tian, Y. T. Zhang, C. X. Shan, X. J. Li, *Chem. Mater.* **2019**, *31*, 3917.

[45] F. Zhang, Z. F. Shi, S. Li, Z. Z. Ma, Y. Li, L. T. Wang, D. Wu, Y. T. Tian, G. T. Du, X. J. Li, C. X. Shan, *ACS Appl. Mater. Interfaces* **2019**, *11*, 28013.

[46] J. Cao, S. X. Tao, P. A. Bobbert, C. P. Wong, N. Zhao, *Adv. Mater.* **2018**, *30*, 1707350.

[47] P. K. Nayak, M. Sendner, B. Wenger, Z. P. Wang, K. Sharma, A. J. Ramadan, R. Lovrincic, A. Pucci, P. K. Madhu, H. J. Snaith, *J. Am. Chem. Soc.* **2018**, *140*, 574.

[48] Q. Chen, L. Chen, F. Y. Ye, T. Zhao, F. Tang, A. Rajagopal, Z. Jiang, S. L. Jiang, A. K. Y. Jen, Y. Xie, J. H. Cai, L. W. Chen, *Nano Lett.* **2017**, *17*, 3231.

[49] S. Shahbazi, C. M. Tsai, S. Narra, C. Y. Wang, H. S. Shiu, S. Afshar, N. Taghavinia, E. W. G. Diau, *J. Phys. Chem. C* **2017**, *121*, 3673.

[50] M. Abdi-Jalebi, M. Pazoki, B. Philippe, M. I. Dar, M. Alsari, A. Sadhanala, G. Diyitini, R. Imani, S. Lilliu, J. Kullgren, H. Rensmo, M. Grätzel, R. H. Friend, *ACS Nano* **2018**, *12*, 7301.

[51] M. Abdi-Jalebi, M. I. Dar, A. Sadhanala, S. P. Senanayak, M. Franckevicius, N. Arora, Y. Y. Hu, M. K. Nazeeruddin, S. M. Zakeeruddin, M. Gratzel, R. H. Friend, *Adv. Energy Mater.* **2016**, *6*, 1502472.

[52] M. Lu, X. Y. Zhang, X. Bai, H. Wu, X. Y. Shen, Y. Zhang, W. Zhang, W. T. Zheng, H. W. Song, W. W. Yu, A. L. Rogach, *ACS Energy Lett.* **2018**, *3*, 1571.

[53] W. Z. Xu, L. Y. Zheng, X. T. Zhang, Y. Cao, T. Y. Meng, D. Z. Wu, L. Liu, W. P. Hu, X. Gong, *Adv. Energy Mater.* **2018**, *8*, 1703178.

[54] C. Caddeo, D. Marongiu, S. Meloni, A. Filippetti, F. Quochi, M. Saba, A. Mattoni, *Adv. Mater. Interfaces* **2019**, *6*, 1801173.

[55] L. G. Gao, L. K. Wang, X. G. Ding, E. L. Zhao, S. Z. Yang, Y. Y. Zhao, Y. Q. Li, S. F. Wang, T. L. Ma, *J. Mater. Chem. A* **2018**, *6*, 4365.

[56] J. Haruyama, K. Sodeyama, L. Y. Han, Y. Tateyama, *J. Phys. Chem. Lett.* **2014**, *5*, 2903.

[57] J. Xu, A. Buin, A. H. Ip, W. Li, O. Voznyy, R. Comin, M. J. Yuan, S. Jeon, Z. J. Ning, J. J. McDowell, P. Kanjanaboos, J. P. Sun, X. Z. Lan, L. N. Quan, D. H. Kim, I. G. Hill, P. Maksymovych, E. H. Sargent, *Nat. Commun.* **2015**, *6*, 7081.

[58] E. Mosconi, J. M. Azpiroz, F. De Angelis, *Chem. Mater.* **2015**, *27*, 4885.

[59] J. Kim, S. H. Lee, J. H. Lee, K. H. Hong, *J. Phys. Chem. Lett.* **2014**, *5*, 1312.

[60] J. Haruyama, K. Sodeyama, L. Y. Han, Y. Tateyama, *J. Am. Chem. Soc.* **2015**, *137*, 10048.

[61] M. I. Saidaminov, J. Kim, A. Jain, R. Quintero-Bermudez, H. R. Tan, G. K. Long, F. R. Tan, A. Johnston, Y. C. Zhao, O. Voznyy, E. H. Sargent, *Nat. Energy* **2018**, *3*, 648.

[62] E. M. Tennyson, B. Roose, J. L. Garrett, C. Gong, J. N. Munday, A. Abate, M. S. Leite, *ACS Nano* **2019**, *13*, 1538.

[63] X. P. Zheng, Y. Hou, H. T. Sun, O. F. Mohammed, E. H. Sargent, O. M. Bakr, *J. Phys. Chem. Lett.* **2019**, *10*, 2629.

[64] Q. Dong, L. Lei, J. Mendes, F. So, *J. Phys. Mater.* **2020**, *3*, 012002.

[65] J. J. Zhao, Y. H. Deng, H. T. Wei, X. P. Zheng, Z. H. Yu, Y. C. Shao, J. E. Shield, J. S. Huang, *Sci. Adv.* **2017**, *3*, eaao5616.

[66] Z. Ma, Z. Shi, D. Yang, F. Zhang, S. Li, L. Wang, D. Wu, Y. Zhang, G. Na, L. Zhang, X. Li, Y. Zhang, C. Shan, *ACS Energy Lett.* **2020**, *5*, 385.

[67] T. Du, J. Kim, J. Ngiam, S. Xu, P. R. F. Barnes, J. R. Durrant, M. A. McLachlan, *Adv. Funct. Mater.* **2018**, *28*, 1801808.

[68] K. Wang, Y. T. Shi, L. G. Gao, R. H. Chi, K. Shi, B. Y. Guo, L. Zhao, T. L. Ma, *Nano Energy* **2017**, *31*, 424.

[69] O. Almora, I. Zarazua, E. Mas-Marza, I. Mora-Sero, J. Bisquert, G. Garcia-Belmonte, *J. Phys. Chem. Lett.* **2015**, *6*, 1645.

[70] S. J. Clark, M. D. Segall, C. J. Pickard, P. J. Hasnip, M. J. Probert, K. Refson, M. C. Payne, *Z. Kristallogr.* **2005**, *220*, 567.

↖↖ **These are not the final page numbers!**

ChemSusChem

Full Papers
doi.org/10.1002/cssc.202000192

Chemistry
Europe
European Chemical
Societies Publishing

FULL PAPERS

Stable ion doping! The effect of Ag doping on the stability of organometal halide perovskites was investigated. Ag doping improves the chemical stability of perovskites against moisture and heat. The improved stability was attributed to morphological and thermodynamic changes.

Ag-doped organometal halide perovskite
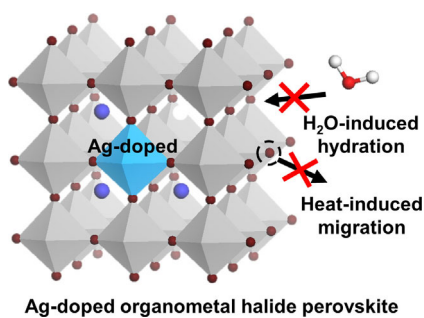
C. Park, S. J. Yang, J. Choi, S. Song, W. Choi, K. Cho*

■■ – ■■

Improved Chemical Stability of Organometal Halide Perovskite Solar Cells Against Moisture and Heat by Ag Doping

These are not the final page numbers! ↗↗